Research Square

Preprints are preliminary reports that have not undergone peer review.
They should not be considered conclusive, used to inform clinical practice,
or referenced by the media as validated information.

Design, Additive Fabrication, and Prototype Validation of 3D-Printed PETG Microalgal Curtain-Wall Modules with Embedded Control

Bi Sheng
Jiangsu Urban and Rural Construction College
Yucheng Guo
Hong Kong Polytechnic University
Mingyang Feng
China Construction Eighth Engineering Division (China)
Yulong Chen
University College London
Xinyi Zheng
Columbia University
Lingxiao Chen
Xi'an University of Posts and Telecommunications
Cossima Cornadó Bardón
Universitat Politècnica de Catalunya
Zeyu Chao
zeyu.chao@upc.edu

Universitat Politècnica de Catalunya
Dingwen Bao
RMIT University
Oriol Pons Valladares
Universitat Politècnica de Catalunya

Article

Keywords: bio-reactive façade, building envelope, photobioreactor, additive manufacturing, parametric design

Posted Date: November 9th, 2026

DOI: https://doi.org/10.21203/rs.3.rs-11403689/v1

License: This work is licensed under a Creative Commons Attribution 4.0 International License.
Read Full License

Additional Declarations: No competing interests reported.

Design, Additive Fabrication, and Prototype Validation of 3D-Printed PETG Microalgal Curtain-Wall Modules with Embedded Control

Sheng Bi[1], Yucheng Guo[3], Mingyang Feng[4], Yulong Chen[5], Xinyi Zheng[6], Lingxiao Chen[7], Cossima Cornadó Bardón[2], Zeyu Chao[2]*, Dingwen Bao[8]*, Oriol Pons Valladares[2]

[1] Jiangsu Urban and Rural Construction Vocational College, Changzhou, Jiangsu, China.

[2] Barcelona School of Architecture (ETSAB), Universitat Politècnica de Catalunya (UPC), Barcelona, Spain.

[3] Department of Building and Real Estate, The Hong Kong Polytechnic University, Hong Kong SAR, China.

[4] China Construction Eighth Engineering Division Co., Ltd., Shanghai, China.

[5] University College London (UCL), London, United Kingdom.

[6] Columbia University, New York, NY, United States.

[7] Xi'an University of Posts and Telecommunications, Xi'an, China.

[8] School of Architecture and Urban Design, RMIT University, Melbourne, VIC, Australia.

Corresponding Authors:Zeyu Chao (Zeyu.chao@upc.edu), Dingwen Bao(nic.bao@rmit.edu.au)

Abstract

Building-integrated photobioreactors require façade components that reconcile geometric adaptability, manufacturability, liquid containment, modularity, and operational monitoring. This study develops a 3D-printed PETG microalgal curtain-wall module integrating parametric design, additive fabrication, embedded sensing, and prototype operation. Nine Rhino/Grasshopper-generated variants (150 × 150 mm) exhibited closed-mesh areas of 707.0–729.4 cm² and predicted filament demand of 29.75–30.54 g (CV 0.87%). Recorded printing times ranged from 100 to 125 min (CV 7.87%). A continuous single-wall spiral-vase strategy enabled transparent reactor prototypes for liquid filling and circulation. An STM32-based system provided multi-source sensing and rule-based pump actuation. Prototype tests showed liquid containment, pump-driven circulation with Spirulina (Arthrospira) culture medium, and preliminary multi-module assembly. The results establish the prototype-level building-engineering feasibility of additively manufactured bio-reactive curtain-wall modules while identifying the requirements for future façade-scale performance validation.

Keywords: bio-reactive façade; building envelope; photobioreactor; additive

manufacturing; parametric design

1.Introduction

Building envelopes are increasingly evolving from passive environmental separators into active components capable of participating in exchanges of energy [1], [2], [3], matter, and information. Microalgal photobioreactors (PBRs) represent one pathway toward such bio-reactive building systems, because a transparent reactor can simultaneously form part of the building skin and provide a controlled space for culture circulation, gas exchange, and microalgal growth[4], [5] . Once translated from a laboratory vessel into a curtain-wall component[6], [7], however, the design problem extends beyond cultivation performance to include geometry, fabrication, liquid containment, modular connection, sensing, maintenance, and operational control[8], [9].

Most existing building-integrated PBRs rely on glass, acrylic, or other transparent sheet materials assembled through machining, bonding, and mechanical connection[10], [11]. These systems provide established solutions for transparency and façade construction but offer comparatively limited flexibility for complex geometries, localized surface modulation, integrated fluidic features, and rapid design iteration[12], [13]. Additive manufacturing provides an alternative by enabling digitally defined geometries to be translated directly into layer-wise fabrication[14], [15] . For liquid-containing components, however, printability alone does not guarantee functional operability[16], [17]. Local curvature, wall thickness, toolpath continuity, seam formation, and fabrication strategy can influence both manufacturing stability and liquid containment, while fabrication constraints in turn limit the feasible geometric design space[18], [19].

A further challenge arises from operation. Bio-reactive façade components require the monitoring of changing physical and water-quality conditions and, potentially, the conversion of these signals into actuator commands[20], [21] . Without embedded sensing and control, a digitally fabricated reactor remains largely a passive vessel requiring external monitoring and manual intervention. Integrating sensing, signal processing, and actuation at the component level therefore provides a means of extending the fabricated module toward a cyber-physical building element[22], [23].

Although parametric design, additive manufacturing, and microalgal PBRs have each been widely investigated, comparatively less attention has been paid to the engineering continuity through which a computationally defined geometry is translated into a manufacturable toolpath, physically fabricated as a liquid-containing reactor, equipped with embedded sensing and control, and operated as an integrated prototype. Existing studies frequently emphasize biological performance, environmental potential, or individual fabrication techniques, whereas the connections among geometry generation,

toolpath planning, machine execution, embedded control, and prototype operation remain less systematically addressed[24], [25], [26].

Accordingly, this study investigates the prototype-level building-engineering feasibility of 3D-printed PETG microalgal curtain-wall modules. Rather than optimizing oxygen generation, CO_2 fixation, or biomass productivity, the study focuses on the coordinated realization of geometric adaptability, additive manufacturability, fabrication consistency, liquid containment and circulation, modular assembly, and component-level monitoring and control. Nine parametric geometric variants are used to evaluate morphological differentiation and fabrication demand, while transparent PETG prototypes are employed for liquid-filling, circulation, and preliminary multi-module assembly trials. An embedded sensing-and-control system is incorporated as an operational subsystem to support state acquisition and rule-based pump actuation. As summarized in Fig. 1, the principal contribution is the establishment of an integrated route for translating a digitally designed bio-reactive façade concept into a manufacturable, operable, and modular curtain-wall prototype, while explicitly defining the remaining requirements for future façade-scale performance validation.

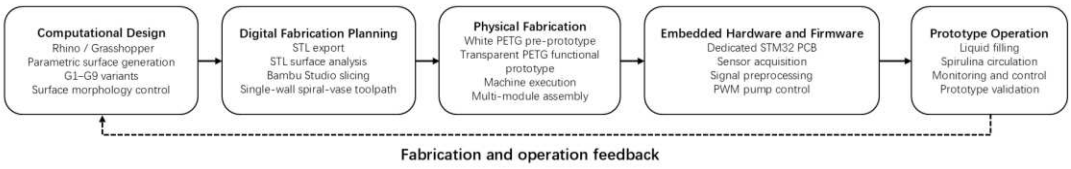


Fig. 1. Integrated workflow linking parametric design, additive manufacturing, embedded control, and prototype operation.

2. Building-Engineering Framework and Evaluation Scope

2.1 From a laboratory photobioreactor to a building-integrated curtain-wall component

A building-integrated photobioreactor is not a single-discipline system, but rather a multi-layered engineering object involving biological processes, building construction, digital fabrication, and embedded control[27], [28] . From a biological perspective, the PBR provides a controlled environment for culture circulation, illumination, and gas exchange. From a building-system perspective, it must additionally satisfy component-level requirements related to scale, interfaces, assembly, connection, and maintenance. From a fabrication perspective, complex surfaces must be translated into continuous and executable deposition paths. From an automation perspective, physical states must be sensed, processed, and further converted into actionable control commands[29], [30]. On this basis, the present study adopts a systems-engineering perspective in which

computational geometry, digital fabrication, sensing, and actuation are treated as consecutive stages within a single workflow rather than as isolated functional subsystems.

Accordingly, the primary evaluation criteria in this study are workflow continuity, inter-component interface relationships, and prototype-level engineering feasibility, rather than final code-compliant façade performance or optimized biological productivity. Engineering feasibility is defined here by the extent to which a parametric definition can generate manufacturable modules with explicit construction logic; a digital model can be translated into a PETG reactor chamber through a consistent slicing and deposition strategy; the fabricated transparent module can support liquid filling and circulation; a dedicated embedded system can acquire relevant operating signals and drive a pump actuator; and the data and physical interfaces linking design, fabrication, sensing, and actuation can be clearly traced within the same system. The study therefore evaluates an end-to-end engineering implementation route for a bio-reactive curtain-wall component, rather than providing final proof of regulatory compliance or biological performance optimization.

2.2 Evaluation criteria and prototype boundaries

The engineering evidence used in this study is derived from four primary sources. The first comprises the Rhino/Grasshopper parametric definition and nine exported STL variants, which are used to examine the geometry-generation logic and morphological differentiation among design alternatives. The second consists of Bambu Studio slicing records, from which predicted filament demand, slicer-predicted printing time, and toolpath-related fabrication parameters are extracted under unified manufacturing settings. These digital fabrication records are complemented by experimentally recorded machine times obtained during physical printing under a common accelerated operating mode. The third source includes the dedicated STM32-based control schematic, the breadboard-based prototype hardware setup, and the associated Keil firmware project, which together provide evidence of the implemented sensing, signal-processing, visualization, and actuator-control pathways. The fourth source comprises physical documentation and operational observations of white PETG manufacturing pre-prototypes, transparent PETG functional prototypes, liquid-filling and circulation trials, and multi-module assembly, thereby providing prototype-level evidence for the complete design–fabrication–control–operation chain.

In the geometric analysis, the total surface area of each closed STL mesh is used as a comparative descriptor of geometric development among the parametric variants. This quantity is treated exclusively as a geometric metric and should not be interpreted as an experimentally determined microalgal attachment area or biologically active surface area.

Likewise, filament mass and printing time reported by Bambu Studio are software-predicted quantities obtained under consistent slicing conditions and are used to characterize relative fabrication demand at the digital-planning stage. By contrast, the recorded 100–125 min printing times represent physical machine execution under a common Ludicrous operating mode. Because the slicer predictions and physical machine times correspond to different execution-speed conditions, they are not treated as a direct prediction–measurement accuracy comparison.

The embedded control system is evaluated within similarly explicit implementation boundaries. At the schematic level, interfaces are provided for pH, TDS, turbidity, CO_2-related analog input, temperature, liquid level/depth, circulation flow, local OLED visualization, and pump actuation. The corresponding hardware architecture was functionally evaluated through a breadboard-based prototype setup rather than a finalized fabricated PCB. The current firmware implements temperature acquisition, four-channel analog ADC acquisition, interrupt-based flow-pulse counting, signal conversion and preprocessing, local data visualization, and PWM-based circulation-pump actuation. The liquid-level/depth channel remains a reserved hardware interface, while the CO_2 channel currently provides raw ADC acquisition without sensor-specific conversion to calibrated concentration values.

Accordingly, the study distinguishes among designed hardware capability, physically implemented prototype hardware, and functions actively executed in firmware. The presence of an interface in the schematic is not interpreted as evidence that the corresponding sensing or closed-loop function has been fully implemented or experimentally validated. Only functions that are actively acquired, processed, displayed, or actuated by the current prototype are discussed as operational capabilities. The present system should therefore be regarded as a prototype-level cyber-physical implementation rather than a fully autonomous or biologically optimized process-control system.

3. Parametric Computational Design and Geometric Variants

3.1 Grasshopper-based parametric generation

The digital geometry of the reactor modules was developed in Rhino 8 using a Grasshopper-based parametric definition[31], [32]. As illustrated in Fig. 2(a), the computational workflow consisted of surface discretization, noise-field generation, numerical remapping, displacement-amplitude control, and geometric reconstruction. Rather than prescribing a fixed corrugation pattern, the definition was designed to control the amplitude, spatial frequency, and distribution of local surface undulations through a common generative logic. This approach enabled morphologically differentiated surface

configurations to be produced while maintaining consistent geometric boundary conditions for subsequent module extraction and fabrication.

The parametric design state can be expressed as:

(1)

$$\theta = [A, f_n, N_u, N_v, \dots]^T$$

where Adenotes the displacement amplitude, $f_n$represents the spatial scale or frequency parameter of the noise field, and $N_u$and $N_v$define the discretization resolution of the base surface along its two parametric directions. Additional parameters control numerical remapping, geometric scaling, and local morphological characteristics. The generated geometry can therefore be represented as:

(2)

$$G = \mathcal{G}(\theta)$$

For a discretized point $P_i$on the base surface, with corresponding unit normal vector $N_i$and normalized noise value n_i, the local geometric transformation can be expressed as:

(3)

$$P_i' = P_i + An_iN_i$$

and the corresponding displacement magnitude is:

(4)

$$\|P_i' - P_i\| = A \mid n_i \mid$$

As illustrated in Fig. 2(b), the continuously generated parametric surface was subsequently subjected to a geometric subdivision and module-extraction process. Representative surface regions were cropped or bounded according to predefined module dimensions, allowing the continuous morphological field to be translated into discrete component-scale geometries. The purpose of this step was to establish a consistent transition from a continuous parametric surface to manufacturable module units, rather than to compare the final G1–G9 variants. The nine formal geometric variants used for subsequent quantitative comparison are introduced separately in Section 3.2.

The above expressions describe the computational mechanism of geometry generation rather than predictive models of fluid behaviour, optical performance, or microalgal attachment. Displacement amplitude and the spatial distribution of the noise field determine the visible surface modulation, whereas downstream fabrication requirements impose additional constraints on the feasible parameter space. In particular, local curvature, spacing between adjacent surface regions, module boundaries, and the requirement for a continuous executable toolpath constrain the acceptable degree of geometric variation[33], [34] . The design process is therefore treated not as a purely one-directional parameter-to-form operation, but as a manufacturability-constrained geometry-generation and module-extraction process.

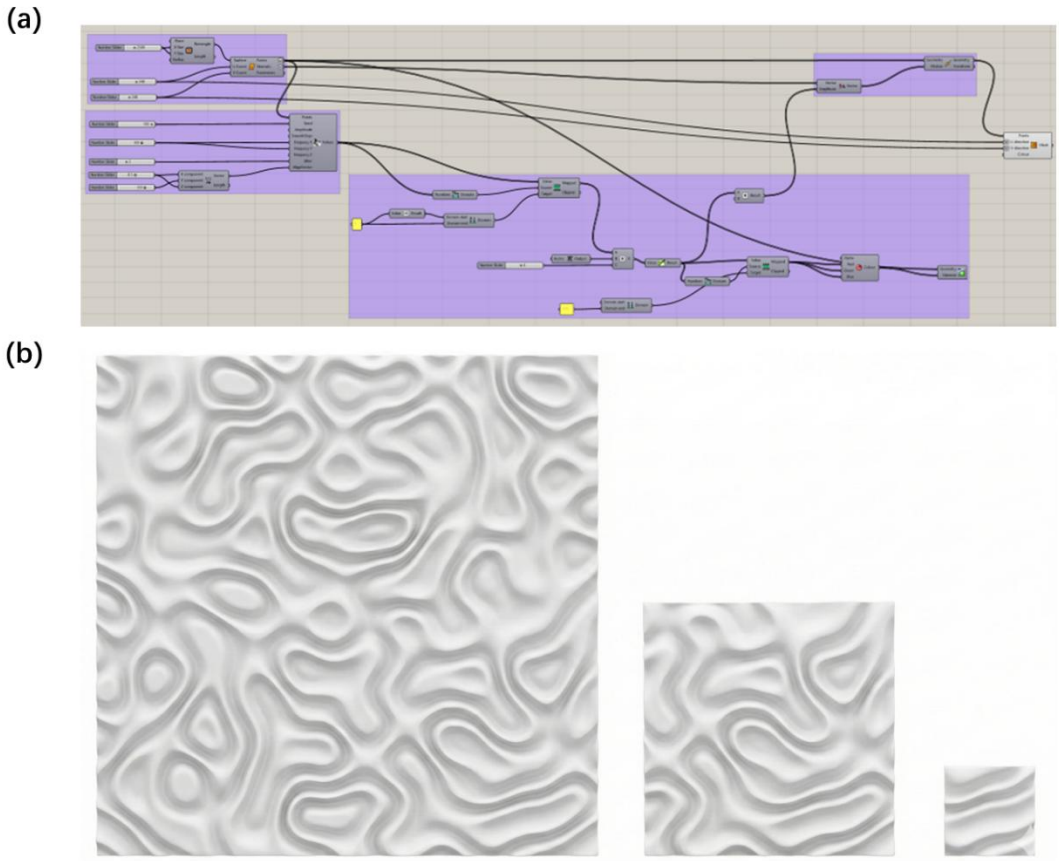


Fig. 2. Grasshopper-based parametric generation and module-extraction process. (a) Parametric definition integrating surface discretization, noise-field generation, numerical remapping, displacement control, and geometric reconstruction; (b) representative geometric subdivision and module-extraction process used to translate the continuous parametric surface into bounded component-scale geometries.

3.2 Nine nominal 150 × 150 mm geometric variants

Nine geometric variants, denoted G1–G9, were generated using the same parametric

definition. All variants were assigned a nominal projected dimension of 150×150mm. Minor deviations were observed in the bounding boxes of the exported STL files; however, these deviations resulted from mesh export and were not intentionally introduced as design variables. They were therefore neglected in the subsequent comparative analysis.

The common nominal projected area was:

$$A_p = 150 \times 150 = 22\,500\ \text{mm}^2 = 225\ \text{cm}^2$$

The total surface areas of the closed STL meshes ranged from 707.0 to 729.4 cm². The relative difference between the maximum and minimum values was calculated as:

(5)

$$\Delta A_s = \frac{A_{s,\max} - A_{s,\min}}{A_{s,\min}} \times 100\%$$

yielding:

$$\Delta A_s = \frac{729.4 - 707.0}{707.0} \times 100\% \approx 3.17\%$$

For normalized comparison among the variants, a surface-development ratio was further defined as:

(6)

$$R_{A,i} = \frac{A_{s,i}}{A_p}$$

where $A_{s,i}$ is the total closed-mesh surface area of variant i, and A_p is the common nominal projected area. Consistent area units were used in calculating $R_{A,i}$. This ratio is intended only as a geometric descriptor of relative surface development among the parametric variants. Because the closed STL surface area includes the principal curved surfaces together with the side and bottom regions, $R_{A,i}$ should not be interpreted as an effective microalgal attachment area or a biologically active surface area.

Table 1. Geometric characteristics and unified slicing results of the nine parametric variants

Variant	STL mesh surface area (cm²)	Predicted filament mass (g)	Slicer-predicted printing time (min)

G1	707.0	29.75	156
G2	714.8	29.92	156
G3	725.8	30.48	156
G4	729.4	30.21	156
G5	710.7	29.90	156
G6	711.4	30.24	156
G7	709.7	30.21	156
G8	723.2	30.23	156
G9	728.2	30.54	156

Despite their visibly distinguishable surface morphologies, the nine variants exhibited only a 3.17% range in total closed-mesh surface area. Under identical slicing conditions, the predicted filament consumption also remained within a narrow range of 29.75–30.54 g, while the slicer-predicted printing time was approximately 156 min for all variants. These results indicate that, within the investigated parameter space, the parametric design system was able to generate morphological differentiation while maintaining a common nominal module scale and highly comparable digital fabrication demand.

It should be noted that the printing times reported in Table 1 represent Bambu Studio predictions under the unified slicing configuration and are therefore used to characterize fabrication planning rather than actual machine execution. The experimentally recorded printing times obtained under a common accelerated machine-side operating mode are analysed separately in Section 4, because the two datasets correspond to different execution-speed conditions and are not treated as a direct slicer-accuracy comparison.

4. Additive-Manufacturing Translation and Fabrication Consistency

4.1 Two-stage PETG prototyping strategy

A two-stage PETG prototyping strategy was adopted to distinguish early manufacturability assessment from later functional-reactor validation. As shown in Fig. 3, the workflow proceeded from a parametric digital model to a white PETG manufacturing pre-prototype and then to a transparent PETG functional prototype, followed by prototype-level operation. In the first stage, white PETG was used to fabricate manufacturing pre-prototypes in order to evaluate whether the curved geometries could be formed continuously, whether local curvature or material shrinkage introduced toolpath discontinuities or visible deformation, and whether module boundaries and

connection regions could be fabricated reliably. Compared with transparent material, the opaque white PETG reduced optical interference caused by reflection and transmission, thereby providing a clearer basis for visual inspection and fabrication-oriented feedback.

After this initial screening, transparent PETG was used to fabricate the functional reactor prototypes. This second stage enabled direct visual observation of liquid filling, internal liquid distribution, and circulation behaviour within the reactor chamber. The white PETG specimens therefore functioned primarily as geometry-to-fabrication validation models, whereas the transparent PETG specimens were further used for liquid-containment observation, circulation testing, and preliminary system-integration assessment. In this sense, the two-stage strategy established a traceable transition from manufacturing-oriented verification to functional prototype implementation, as illustrated by the fabrication-informed iteration indicated in Fig. 3.

The nine parametric variants G1–G9, all treated as nominal 150 × 150 mm modules, were mainly used for morphology comparison and fabrication-consistency analysis under unified slicing conditions. By contrast, the selected transparent functional prototype was further developed at an enlarged scale of approximately 200 × 200 × 50 mm for liquid filling, continuous circulation, and multi-module assembly observations. These two scales therefore served different experimental purposes: the smaller modules supported design-space exploration and comparative fabrication analysis, whereas the enlarged transparent prototype was used for system-level validation of prototype operation.

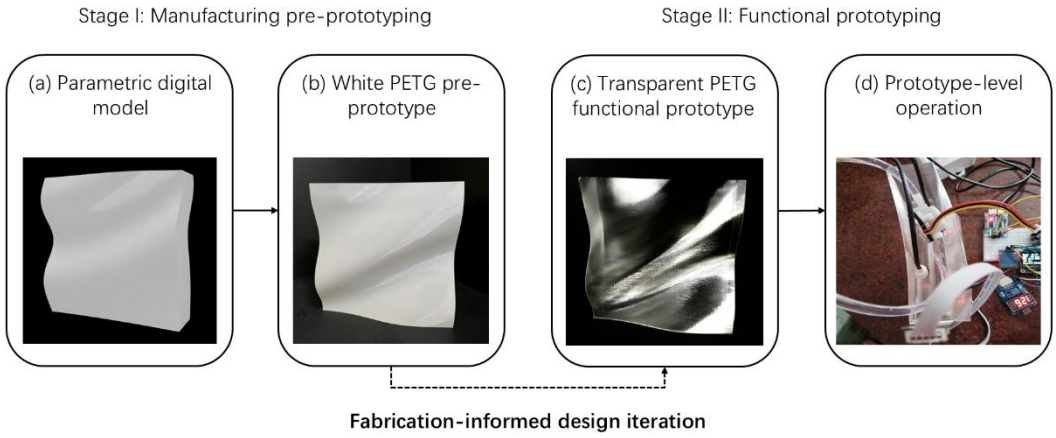


Fig. 3. Two-stage PETG prototyping strategy.
(a) Parametric digital model; **(b)** white PETG manufacturing pre-prototype for manufacturability assessment; **(c)** transparent PETG functional prototype for liquid-state observation and circulation testing; and **(d)** prototype-level operation. The dashed arrow indicates fabrication-informed iteration from pre-prototyping to functional implementation.

4.2 Continuous single-wall toolpath and fabrication consistency

Physical fabrication was conducted using a Bambu Lab P1S fused-deposition-modelling (FDM) printer equipped with a standard 0.4 mm stainless-steel nozzle. The nine parametric variants G1–G9 and the white manufacturing pre-prototypes were fabricated using SUNLU white PETG filament, while the functional reactor prototypes were produced using SUNLU transparent PETG filament. Both materials had a nominal filament diameter of 1.75 mm. During printing, the nozzle temperature was set to 255 °C, while the build-plate temperature was maintained at 70 °C.

Bambu Studio slicing records showed that all nine morphology-screening modules were prepared using a unified continuous single-wall fabrication strategy. A 0.12 mm Fine slicing profile was adopted, with a nominal layer height of 0.12 mm, a first-layer height of 0.20 mm, a default and outer-wall line width of 0.42 mm, and a single wall loop. Spiral-vase mode was enabled, with zero top-shell layers and five bottom-shell layers. This configuration allowed the reactor envelope to be formed predominantly through a continuous outer-shell toolpath, thereby reducing local discontinuities associated with repeated starts, stops, retractions, and seam locations in conventional perimeter-based deposition[35], [36].

Across the nine variants, the outer-wall operation accounted for approximately 91.2%–92.0% of the slicer-predicted model-printing time and 85.1%–86.0% of the predicted filament consumption. The fabrication strategy therefore exhibited a clear shell-dominated character, with most of the planned material and manufacturing time concentrated in the functional envelope rather than in internal infill or support structures.

Table 2. Principal fabrication, slicing, and machine-execution parameters for the nine parametric modules

Parameter	Setting / result
3D printer	Bambu Lab P1S
Printing technology	Fused deposition modelling (FDM)
Nozzle diameter	0.4 mm
Nozzle material	Stainless steel
Filament	SUNLU white PETG
Filament diameter	1.75 mm
Nozzle temperature	255 °C
Build-plate temperature	70 °C

Slicing software	Bambu Studio
Nominal specimen size	150 × 150 mm (G1–G9)
Layer height	0.12 mm
First-layer height	0.20 mm
Default/outer-wall line width	0.42 mm
Wall loops	1
Spiral vase	Enabled
Top shell layers	0
Bottom shell layers	5
Predicted filament mass	29.75–30.54 g/module
Slicer-predicted printing time	approximately 156 min/module
Machine-side operating mode	Ludicrous mode for all variants
Recorded printing time	100–125 min/module
Mean recorded printing time	112 min/module

To evaluate material-demand consistency under identical slicing conditions, the mean predicted filament mass was calculated as:

(7)

$$\bar{m} = \frac{1}{n}\sum_{i=1}^{n} m_i$$

yielding:

$$\bar{m} = 30.16\ \mathrm{g}$$

The corresponding sample standard deviation was:\

(8)

$$s_m = \sqrt{\frac{1}{n-1}\sum_{i=1}^{n}(m_i - \bar{m})^2}$$

with:

$$s_m \approx 0.26\ \mathrm{g}$$

The coefficient of variation was therefore:

$$CV_m = \frac{s_m}{\bar{m}} \times 100\% = 0.87\%$$

and the normalized range of predicted material demand was:

$$\Delta m = \frac{m_{\max} - m_{\min}}{\bar{m}} \times 100\% \approx 2.62\%$$

As shown in Fig. 4(a), the predicted filament consumption remained tightly clustered between 29.75 and 30.54 g across G1–G9. The low coefficient of variation indicates that the visible morphological differences introduced by the parametric system had only a minor effect on predicted material demand within the investigated design space.

To characterize the shell-dominated nature of the fabrication strategy, the outer-shell material ratio of variant $i$was defined as:

(9)

$$R_{\mathrm{shell},i} = \frac{m_{\mathrm{outer},i}}{m_{\mathrm{total},i}} \times 100\%$$

where $m_{\mathrm{outer},i}$is the slicer-predicted filament mass associated with the outer wall and $m_{\mathrm{total},i}$is the total predicted filament mass.

At the digital fabrication-planning stage, Bambu Studio reported an approximately identical model-printing time of 156 min for all nine variants. At the minute-level display resolution of the slicer, the corresponding coefficient of variation can therefore be approximated as:

$$CV_{t,\mathrm{slicer}} \approx 0$$

Physical fabrication was subsequently conducted using the same accelerated machine-side operating strategy for all variants, with Ludicrous mode enabled during printing. The recorded machine times for G1–G9 were 100, 116, 120, 105, 108, 102, 125, 112, and 120

min, respectively. The mean recorded printing time was:

$$\bar{t}_{\text{actual}} = \frac{1}{n}\sum_{i=1}^{n} t_i = 112 \text{ min}$$

with a sample standard deviation of:

$$s_{t,\text{actual}} = \sqrt{\frac{1}{n-1}\sum_{i=1}^{n}(t_i - \bar{t}_{\text{actual}})^2} \approx 8.82 \text{ min}$$

and a coefficient of variation of:

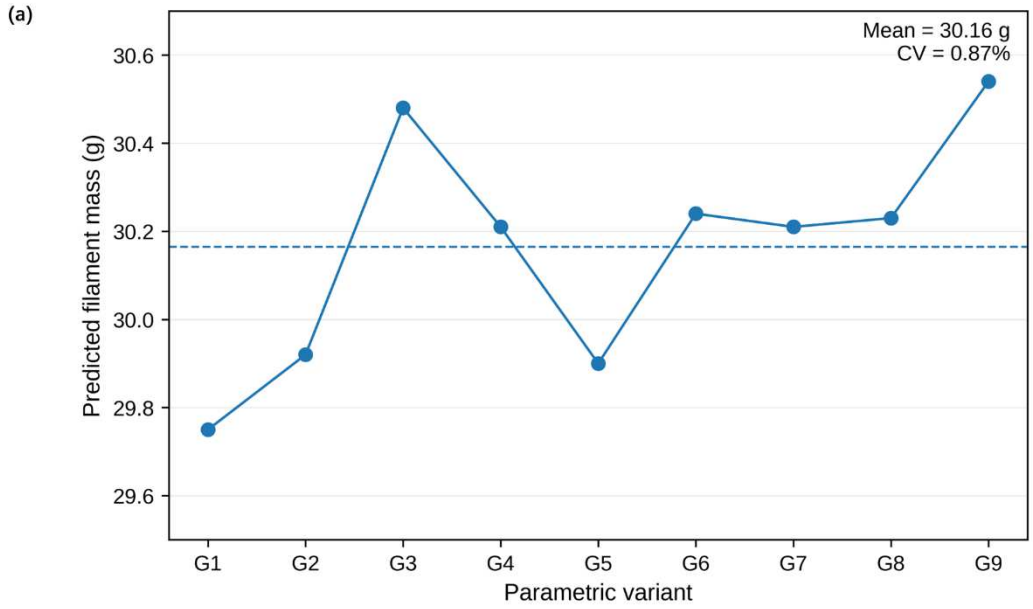
$$CV_{t,\text{actual}} = \frac{s_{t,\text{actual}}}{\bar{t}_{\text{actual}}} \times 100\% \approx 7.87\%$$

The distribution of recorded machine times is shown in Fig. 4(b). Although the physical printing times varied more than the slicer-predicted values, they remained within a relatively narrow range of 100–125 min under the common accelerated operating mode. This indicates that geometric differentiation introduced measurable but limited variation in machine-level execution time.

It is important to distinguish the two time datasets. The approximately 156 min values represent Bambu Studio predictions under the unified slicing configuration, whereas the recorded 100–125 min values correspond to physical machine execution with Ludicrous mode enabled. Because the two datasets were obtained under different machine-speed conditions, their absolute difference is not interpreted as a slicer prediction error. Instead, the slicer data are used to characterize consistency at the digital fabrication-planning stage, while the recorded times characterize variability during actual machine execution.

Taken together, Fig. 4(a–b) demonstrates two complementary aspects of fabrication consistency. At the planning stage, predicted filament consumption varied by less than 1% in coefficient-of-variation terms, while predicted printing time was effectively identical across the nine variants. At the machine-execution stage, actual printing time exhibited a coefficient of variation of 7.87%. These results suggest that, within the investigated parameter space, parametrically differentiated surface morphologies can be produced while maintaining highly consistent material demand and relatively stable production time. For modular façade fabrication, this compatibility between geometric differentiation and repeatable manufacturing demand is more relevant than geometric complexity alone,

because it directly affects material budgeting, scheduling, and the feasibility of repeated component production.



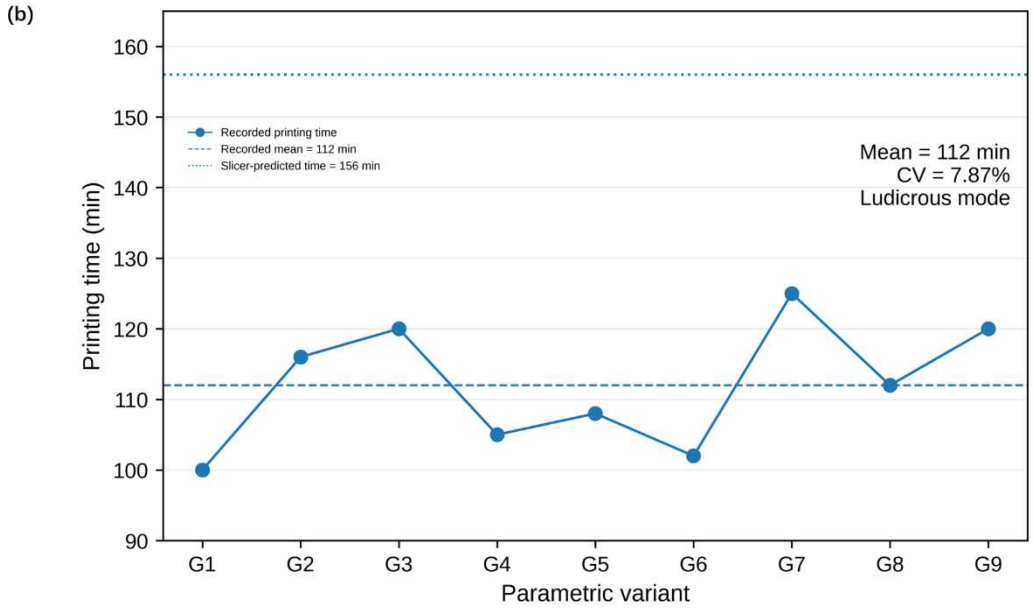


Fig. 4. Digital fabrication demand and physical machine execution across the nine parametric variants.

(a) Slicer-predicted filament consumption under identical slicing conditions, showing a mean value of 30.16 g and a coefficient of variation of 0.87%; (b) recorded printing time under a common Ludicrous machine-side operating mode, with a mean of 112 min and a coefficient of variation of 7.87%. The slicer-predicted printing time of approximately 156 min is shown as a digital-planning reference and is not interpreted as a direct prediction–measurement comparison because the

physical prints were executed under an accelerated machine-side mode.

4.3 Toolpath as an intermediate representation between digital geometry and physical fabrication

The fabrication trials demonstrated that geometric continuity in the CAD environment does not, by itself, guarantee the successful production of a thin-walled reactor chamber. A continuous digital surface must first be translated into a machine-executable deposition path, which is subsequently interpreted and executed under specific printer operating conditions[37], [38]. Toolpath generation was therefore treated as an intermediate representation linking computational geometry and physical fabrication rather than as a passive final-export step. This translation process is illustrated in Fig. 5, which follows a representative module from parametric geometry through slicing and continuous-path generation to the fabricated PETG component.

The overall design-to-fabrication sequence can be expressed as:

(10)

$$G_{\mathrm{digital}} \rightarrow T_{\mathrm{toolpath}} \rightarrow M_{\mathrm{execution}} \rightarrow G_{\mathrm{fabricated}}$$

where G_{digital} represents the computational geometry, T_{toolpath} denotes the machine-oriented deposition path generated by the slicer, $M_{\mathrm{execution}}$ represents the physical execution of that path under the selected machine operating condition, and $G_{\mathrm{fabricated}}$ is the resulting printed component.

As shown in Fig. 5(a–b), the parametric digital geometry is first translated into a slicer-based fabrication representation. At this stage, the resulting toolpath can be expressed conceptually as a function of the digital geometry and principal fabrication parameters:

(11)

$$T_{\mathrm{toolpath}} = \mathcal{T}\left(G_{\mathrm{digital}}, h, w, v, s\right)$$

where h is the layer height, w is the extrusion line width, v represents printing-speed-related slicing parameters, and s describes the seam and path-continuity strategy. In the present study, the spiral-vase configuration played a central role in converting the reactor envelope into a continuous single-wall deposition trajectory. The resulting path continuity is visualized in Fig. 5(c), where the sliced geometry is represented as a continuous outer-shell toolpath rather than as a conventional sequence of discontinuous perimeter segments.

Machine execution constitutes a further stage between the planned toolpath and the fabricated component. This relationship can be represented conceptually as:

(12)

$$M_{\text{execution}} = \mathcal{M}(T_{\text{toolpath}}, \lambda)$$

where λ denotes the machine-side operating condition. In the physical fabrication experiments, the same Ludicrous mode was applied to all nine variants. This distinction between digital fabrication planning and machine execution is important because identical slicer-predicted times do not necessarily result in identical physical printing times. As reported in Section 4.2, the slicer assigned approximately 156 min to all variants, whereas the recorded machine times under the common accelerated operating mode ranged from 100 to 125 min. The fabricated outcome corresponding to this translation chain is represented in Fig. 5(d).

Fabrication was therefore treated as an iterative rather than purely linear process. Observations from the printed components can provide feedback to the acceptable geometric design space:

(13)

$$G_{\text{digital}} \rightarrow T_{\text{toolpath}} \rightarrow M_{\text{execution}} \rightarrow G_{\text{fabricated}} \rightarrow F_{\text{geometry}}$$

where F_{geometry} denotes fabrication-derived feedback related to geometric manufacturability. In the present workflow, this feedback was used to assess whether local surface modulation, boundary transitions, and thin-wall geometry remained compatible with continuous deposition. The transition from the digital model in Fig. 5(a) to the fabricated component in **Fig. 5(d)** therefore represents not only a geometric conversion, but also a sequence of manufacturing decisions mediated by the slicer and the machine-execution stage.

Accordingly, the fabrication workflow is not interpreted as a simple CAD-to-print conversion. Instead, it comprises three distinct but coupled representations: computational geometry defines what is to be produced, the toolpath defines how that geometry is translated into deposition instructions, and machine execution determines how those instructions are physically realized. This distinction is particularly relevant to parametrically differentiated building components, because similar digital fabrication demand does not necessarily imply identical machine-level execution. Treating toolpath generation as an explicit intermediate representation therefore provides a clearer basis for linking computational design decisions to physical manufacturing behaviour[39], [40].

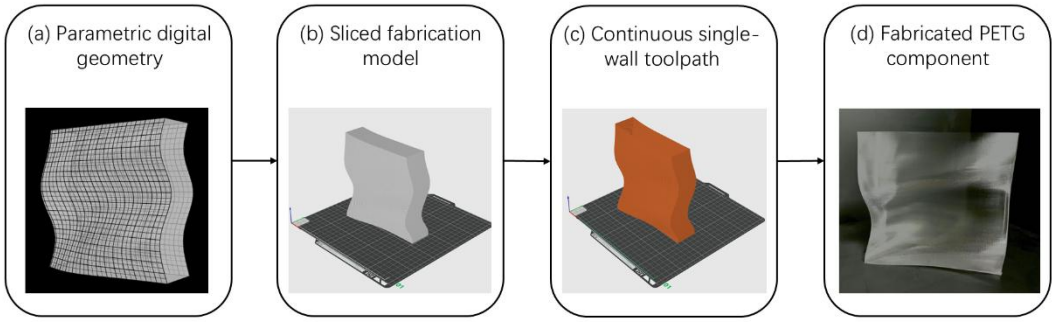


Fig. 5. Geometry-to-toolpath-to-fabrication translation of the PETG reactor module.(a) Representative parametric digital geometry; (b) slicer-translated fabrication model; (c) continuous single-wall toolpath generated using the spiral-vase strategy; and (d) fabricated PETG thin-wall component. The sequence illustrates the role of toolpath generation and machine execution as intermediate stages between computational geometry and physical fabrication.

5. Embedded Monitoring and Operational Control of the PBR Module

5.1 Hardware architecture and sensing interfaces

To support prototype-level operation of the bio-reactive curtain-wall module, an embedded monitoring-and-control system was developed to integrate liquid-state sensing, circulation monitoring, local visualization, and pump actuation. Rather than functioning as a standalone automation platform, the system was incorporated as an operational subsystem of the PETG PBR module, enabling the fabricated reactor to transition from a passive liquid-containing component toward an actively monitored building-envelope prototype.

The system is based on an STM32F103VET6 microcontroller operating at 72 MHz. The power architecture provides DC and USB Type-C input paths, followed by DC–DC conversion to 5 V and regulation to 3.3 V. As illustrated in Fig. 6, the sensing layer incorporates analog interfaces for TDS, turbidity, CO_2-related signals, and pH, together with a DS18B20 temperature sensor and a pulse-based circulation-flow sensor. The controller provides local state visualization through an OLED display and circulation-pump actuation through an L9110S motor driver.

The four analog sensing channels are connected to ADC1 through PA1–PA4, while temperature is acquired through a 1-Wire interface on PB0 and circulation flow through falling-edge pulse counting on PB1/EXTI1. Pump actuation is implemented through TIM4_CH4 on PB9, with PB8 providing the complementary control input to the L9110S driver. A liquid-level/depth interface is additionally retained as a reserved hardware capability for future dry-run protection and level-dependent control. The principal

sensing and actuation interfaces and their current implementation status are summarized in Table 3.

Table 3. Principal sensing, visualization, and actuation interfaces and their current implementation status in the STM32-based embedded control system

Function	MCU/interface	Current implementation status
TDS	PA1 / ADC1	Acquired and converted in firmware
Turbidity	PA2 / ADC1	Acquired and converted in firmware
CO_2	PA3 / ADC1	Raw ADC acquisition; ppm calibration not yet implemented
pH	PA4 / ADC1	Acquired and converted in firmware
Temperature	PB0 / 1-Wire	DS18B20; implemented
Circulation flow	PB1 / EXTI1	Falling-edge pulse counting; implemented
OLED	Dedicated digital interface	Local state visualization
Pump	PB9 (TIM4_CH4) + PB8	PWM actuation through L9110S
Liquid level/depth	Reserved hardware interface	Included at schematic level; not currently used as a closed-loop input

5.2 Prototype hardware implementation and system boundaries

The overall monitoring-and-control architecture is summarized in Fig. 6, which illustrates the functional relationships among the sensing layer, STM32-based controller, local visualization, pump actuation, and the PETG PBR module. Multi-source sensing signals are transferred to the controller through analog, 1-Wire, and interrupt-based interfaces, while the processed system state is used for local display and circulation-pump control. The return path from the reactor module to the sensing layer represents the physical feedback relationship between prototype operation and subsequent state acquisition. In this configuration, the embedded system functions as an operational subsystem of the curtain-wall prototype rather than as an independent automation platform.

The corresponding hardware implementation is shown in Fig. 7. The STM32F103VET6 minimum-system circuitry provides the central platform for sensor acquisition and actuator control, while the breadboard-based setup was used for integrated testing of sensing, local visualization, and circulation-pump actuation. Representative sensing and

actuation interfaces, including the water-quality channels, circulation-flow input, reserved liquid-level/depth interface, and L9110S-based pump driver, are further illustrated in Fig. 7(c). The prototype arrangement was intended for functional integration and was not designed as a finalized production-ready control board.

The degree of implementation differs among the available sensing channels. TDS, turbidity, and pH signals are acquired and converted into firmware-derived values, whereas the CO_2 interface currently provides raw analog acquisition without calibrated ppm conversion. Temperature and circulation flow are implemented through digital and interrupt-based acquisition, respectively. The liquid-level/depth interface remains a reserved hardware capability and does not currently participate in the implemented control loop.

Accordingly, a distinction is maintained between system-level hardware availability and operational functionality. Only signals that are actively acquired, processed, displayed, or used for actuation are treated as implemented functions in the present prototype. This boundary is important because the embedded system is intended to support component-level monitoring and circulation operation of the bio-reactive curtain-wall prototype, rather than to represent a fully autonomous biological-process management platform [41], [42].

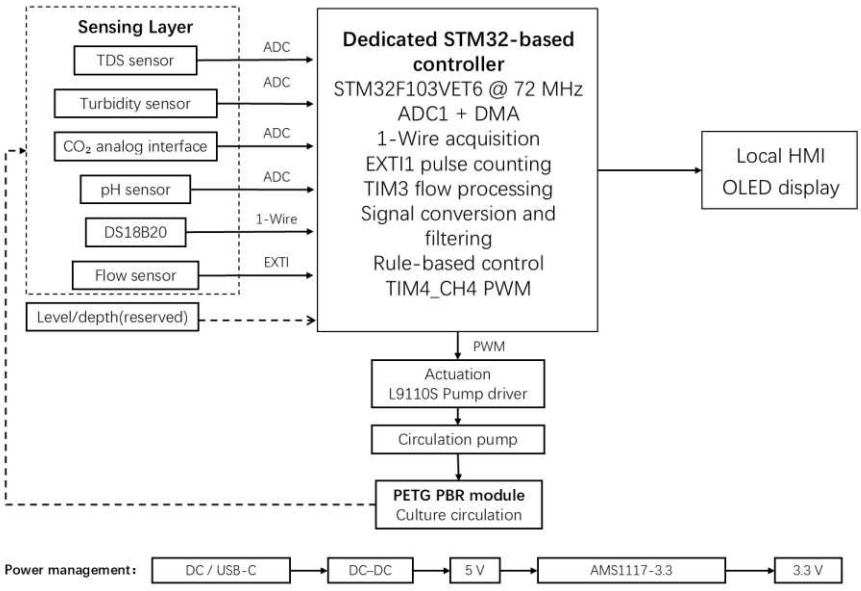


Fig. 6. Embedded monitoring-and-control architecture of the bio-reactive PETG curtain-wall prototype. Multi-source sensing signals are acquired by a dedicated STM32F103VET6-based controller through analog, 1-Wire, and interrupt-based interfaces. The embedded system performs signal acquisition, conversion and filtering, flow processing, rule-based control, local OLED visualization, and PWM-based pump actuation. The liquid-level/depth interface is retained

as a reserved hardware capability, while the dashed return path represents physical-state feedback from the PETG PBR module to the sensing layer.

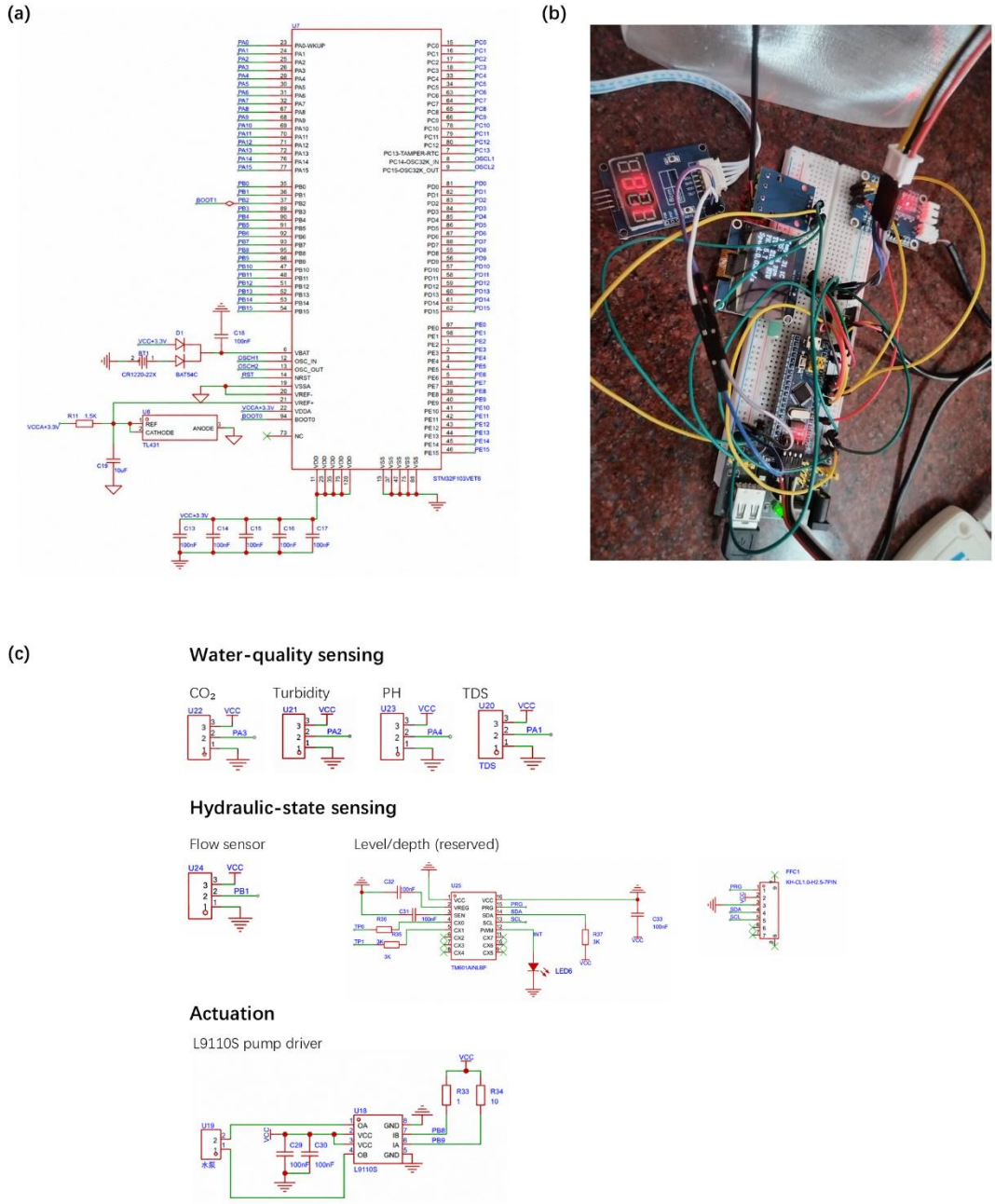


Fig. 7. STM32-based embedded control implementation and prototype hardware integration. (a) STM32F103VET6 MCU core and minimum-system schematic; (b) breadboard-based prototype hardware setup used for integrated sensing, visualization, and actuator testing; and (c) representative sensing and actuation interface circuits, including water-quality sensing channels, flow and reserved liquid-level/depth interfaces, and the L9110S-based circulation-pump driver.

5.3 Signal processing and rule-based circulation control

The implemented sensing–processing–actuation workflow is summarized in Fig. 8. Four analog channels corresponding to TDS, turbidity, CO_2-related input, and pH are continuously acquired through ADC1 and DMA, while temperature is measured using a DS18B20 sensor and circulation flow is obtained through interrupt-based pulse counting. The acquired signals are subsequently converted or preprocessed in firmware to provide operational state information for the prototype.

Temperature compensation is applied to the TDS and turbidity channels, while the pH signal is converted using the linear relationship implemented in the firmware. These outputs are treated as firmware-derived operational values rather than metrologically validated measurements. Sensor-specific calibration against reference solutions or independent instrumentation would therefore be required before quantitative sensing accuracy could be reported. Likewise, the CO_2 interface currently retains the raw ADC signal without conversion to calibrated concentration values.

Circulation flow is acquired through falling-edge pulse counting on PB1/EXTI1 and processed at approximately 200 ms intervals. A five-sample moving average is applied to reduce short-term fluctuations associated with pulse discreteness, transient bubbles, and pump pulsation. Because the pulse-to-flow coefficient was not independently calibrated against a volumetric reference, the resulting signal is interpreted primarily as an indicator of relative circulation state.

The current actuation strategy employs a two-state rule-based controller in which the processed TDS value is used to determine the circulation-pump PWM command. When the TDS value exceeds the commissioning threshold of 50, the pump is operated at 100% PWM; otherwise, a 50% PWM command is applied. This threshold is used solely to demonstrate the sensing–decision–actuation pathway and should not be interpreted as a biologically optimized control threshold for *Spirulina* cultivation.

The implemented control strategy therefore provides a transparent prototype-level link between state acquisition, signal processing, operational decision-making, and physical circulation control. Its purpose is to support the operation and evaluation of the curtain-wall prototype rather than to establish an advanced predictive or biologically optimized control system. More sophisticated control would require calibrated sensing, long-term biological datasets, and validated relationships among circulation, water-quality conditions, illumination, and microalgal response [43], [44].

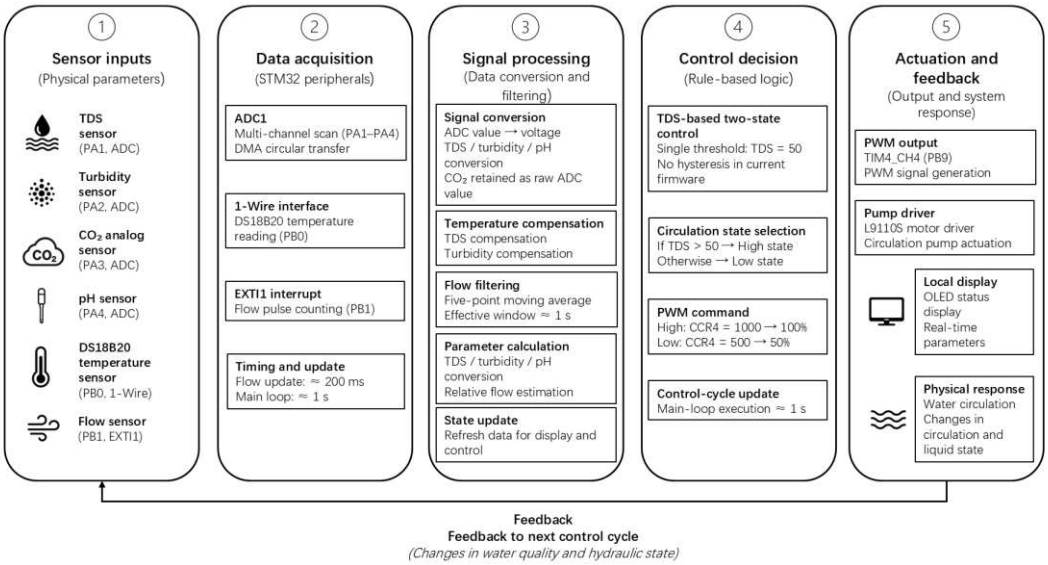


Fig. 8. Firmware sensing–processing–actuation workflow. Multi-source sensor signals are acquired through ADC, 1-Wire, and EXTI1 interfaces and subsequently processed through voltage conversion, temperature compensation, parameter conversion, and flow-signal averaging. The current firmware applies a single-threshold two-state TDS rule, with TDS > 50 corresponding to a 100% pump PWM command and the alternative state corresponding to 50% PWM. CO_2 is retained as a raw analog signal, while the five-point moving average is applied to the flow channel. Pump actuation is implemented through TIM4_CH4 and the L9110S driver, with the resulting physical state returning to the sensing layer in the subsequent control cycle.

6. Prototype-Level Functional Validation for Curtain-Wall Integration

6.1 Liquid containment and geometric stability

Following fabrication, the transparent PETG functional prototype was subjected to liquid-filling trials to evaluate its geometric stability and basic liquid-containment capability. During filling, the overall geometry of the module remained visually stable, with no evident macroscopic deformation or observable leakage. The transparent PETG envelope also enabled direct observation of the internal liquid state, allowing the liquid level and local distribution to be inspected without disassembling the module.

These observations indicate that, at the current prototype scale and under the tested conditions, the continuous single-wall fabrication strategy was capable of producing a thin-walled reactor chamber suitable for subsequent circulation and system-integration trials. However, the assessment remained qualitative and did not follow standardized procedures for curtain-wall watertightness, long-term leakage, hydrostatic-pressure resistance, or pressure-vessel performance [45]. The results should therefore be interpreted as preliminary evidence of prototype-level containment feasibility rather than

as certified watertightness or structural performance.

6.2 Circulation operation with *Spirulina*-containing culture medium

Following the liquid-filling assessment, the transparent PETG reactor chamber was operated with a *Spirulina* (*Arthrospira*)-containing culture medium under pump-driven circulation. As shown in Fig. 9, this stage examined whether the additively manufactured reactor chamber could accommodate the culture medium, maintain observable recirculation, and operate together with the embedded monitoring-and-control subsystem.

During the observation period, pump-driven liquid movement was maintained within the transparent module, and the prototype remained operational under the tested conditions. The culture medium exhibited a generally distributed colour appearance, while no obvious large-scale accumulation or complete flow blockage was visually observed. These observations indicate functional compatibility among the printed reactor geometry, fluid interfaces, circulation hardware, and operational subsystem, extending the validation from static liquid containment to active prototype operation.

The present evidence nevertheless remains qualitative rather than biological or hydrodynamic. Biomass concentration, growth rate, dissolved oxygen, CO_2 fixation, photosynthetic efficiency, residence time, internal velocity distribution, and long-term cultivation stability were not quantitatively measured [46], [47]. Fig. 9 should therefore be interpreted as evidence of prototype-level circulation feasibility and system integration rather than as proof of optimized flow distribution, biological productivity, oxygen-generation performance, or environmental benefit.

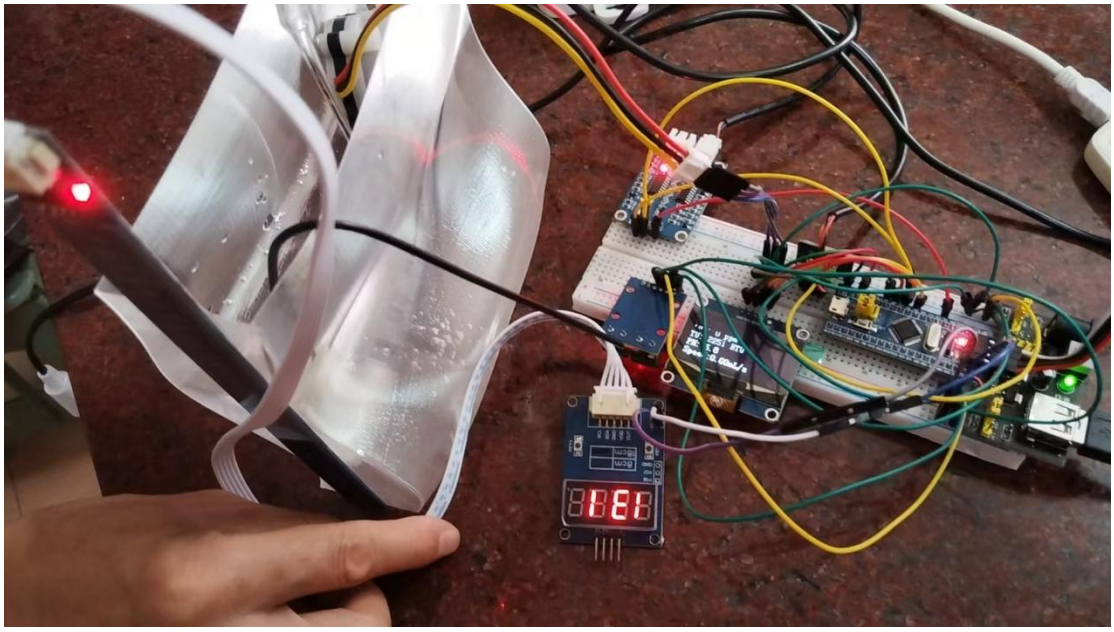


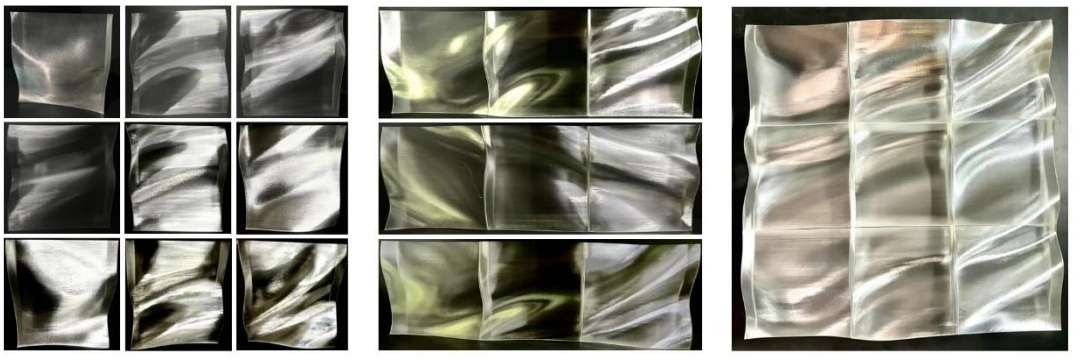
Fig. 9. Prototype-level circulation operation of the transparent PETG PBR module containing *Spirulina* culture medium. The image illustrates the integrated operation of the additively manufactured transparent reactor chamber, circulation tubing, and embedded monitoring-and-control subsystem during pump-driven circulation.

6.3 Modular assembly and façade integration potential

To examine the transition from an individual reactor chamber toward a modular façade configuration, multiple transparent PETG modules were assembled in parallel. As shown in Fig. 10(a,b), the assembly was used to assess dimensional coordination among repeated units, visual continuity across adjacent modules, and the potential for arranging parametrically differentiated components within a repeated curtain-wall configuration.

The prototype assembly demonstrates that modules with different surface geometries can be combined into a coherent array when common module boundaries and nominal dimensional constraints are maintained. This result indicates that the parametric design approach can support not only individual reactor components but also a modular aggregation strategy in which geometric differentiation is introduced without compromising overall spatial continuity and assembly coherence.

The current assessment remains limited to prototype-scale assembly rather than building-scale façade validation. The modules were operated primarily as relatively independent units, while requirements including shared supply and return lines, inter-module hydraulic balancing, venting and drainage, curtain-wall sub-frame connection, maintenance access, and centralized or distributed control have not yet been experimentally verified [48], [49]. The multi-module configuration should therefore be interpreted as preliminary evidence of modular scalability and façade-integration potential rather than as complete validation of a building-scale PBR curtain-wall system.



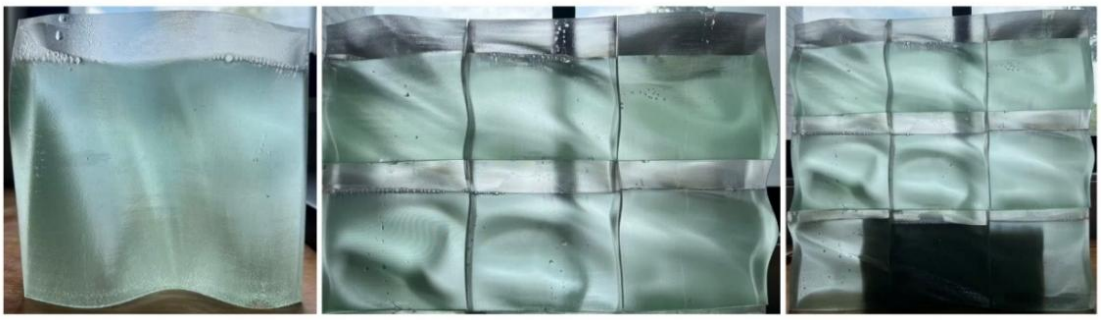


Fig. 10. Multi-module assembly and façade-integration potential of the transparent PETG PBR modules.
(a) Prototype assembly of multiple transparent modules;
(b) façade-like arrangement illustrating dimensional coordination and visual continuity among repeated units.

7. Discussion

7.1 Additive manufacturability of parametrically differentiated façade modules

The fabrication results demonstrate that controlled geometric differentiation can be introduced into PETG curtain-wall modules while maintaining relatively stable manufacturing demand within the investigated design space. Across G1–G9, the total closed-mesh surface area varied by approximately 3.2%, while the coefficient of variation in predicted filament consumption was only 0.87%. Recorded machine-execution times ranged from 100 to 125 min, with a coefficient of variation of 7.87%. These results indicate that the morphological differentiation generated by the parametric system did not result in substantial changes in material demand or production time under the adopted fabrication conditions.

This finding should nevertheless be interpreted within the tested geometric range. All variants shared common nominal dimensions and were fabricated using the same continuous single-wall strategy. More extreme curvature, overhang, or local geometric discontinuity may generate different machine responses or fabrication failures. The present results therefore demonstrate compatibility between parametric differentiation and repeatable production under the investigated conditions rather than a general independence of fabrication demand from geometric complexity [50], [51] .

The spiral-vase strategy was central to the fabrication of the thin-walled reactor envelope because it reduced repeated starts, stops, retractions, and seam formation. At the same time, the single-wall configuration provides limited structural redundancy and should therefore be regarded as a prototype fabrication approach rather than a final curtain-wall construction solution [52], [53]. Translation toward façade-scale implementation

would require a fabrication strategy capable of reconciling geometric adaptability with structural resistance, sealing, durability, and long-term service requirements.

7.2 From a printed reactor to an operational façade component

The embedded monitoring-and-control subsystem extends the additively manufactured reactor from a passive liquid-containing prototype toward an operational façade component [54], [55]. Multi-source sensing, local state representation, circulation monitoring, and pump actuation are integrated within a common hardware–software framework, allowing the physical state of the reactor to be acquired, processed, and translated into basic operational responses.

The present implementation nevertheless represents an initial operational layer rather than a fully autonomous biological-process management system. Some sensing interfaces remain reserved at the hardware level, the CO_2 channel is not yet converted into calibrated concentration values, and the circulation pump is the only actuator currently incorporated into the control logic. The two-state TDS-threshold rule should therefore be understood as a commissioning strategy for demonstrating the sensing–processing–actuation pathway rather than as an optimized control strategy for microalgal cultivation.

Within the context of a building-envelope component, the significance of the embedded subsystem lies primarily in its ability to support monitoring and circulation operation within the same physical module. More advanced operational control would require calibrated sensing, long-term datasets, and validated relationships among water-quality conditions, circulation behaviour, illumination, and biological response [56], [57].

7.3 Implications for modular bio-reactive curtain-wall systems

The combined fabrication, liquid-containment, circulation, and assembly results suggest a potential route for translating microalgal photobioreactors from isolated reactor vessels into digitally differentiated building-envelope components. In contrast to conventional PBR configurations based primarily on planar transparent panels, additive manufacturing enables local geometric modulation and rapid digital variation while maintaining common component boundaries and fabrication logic. This creates opportunities for modular façade systems in which individual units share a consistent construction framework while retaining differentiated surface geometries.

The proposed approach should not be interpreted as demonstrating the superiority of PETG over conventional glass- or acrylic-based PBR façades. Rather, it identifies an alternative design and fabrication pathway in which geometric customization, additive manufacturing, modular aggregation, and embedded operational support are

incorporated within a common component concept. At the same time, this flexibility introduces additional requirements associated with structural resistance, sealing, optical performance, weathering, durability, fire safety, hydraulic coordination, and maintenance, all of which must be addressed before building-scale application.

From a building-engineering perspective, the relevance of the proposed system therefore lies not only in the fabrication of an unconventional reactor geometry, but also in the possibility of coordinating geometric variation, manufacturing logic, operational monitoring, and modular assembly within a repeatable façade-component framework. The present prototype provides an initial basis for this integration, while subsequent work must determine whether these advantages can be maintained under the performance requirements imposed on actual building envelopes.

7.4 Limitations and requirements for façade-scale validation

The present study demonstrates prototype-level engineering integration rather than optimized biological or building-envelope performance. Although the parametric surface modulation provides a means of generating differentiated reactor geometries, relationships among surface morphology, hydrodynamic shear, optical transmission, biofilm development, and microalgal productivity were not quantified. Establishing these relationships will require further investigation through fluid-dynamic analysis, optical characterization, surface assessment, and biological monitoring.

Scaling the approximately 200 × 200 × 50 mm functional prototype toward a building-integrated curtain-wall system would introduce additional requirements related to structural loading, standardized watertightness, weathering, ultraviolet exposure, fire performance, sealing, maintenance, hydraulic balancing, drainage, and sub-frame integration [58], [59] [60], [61]. The present study also does not provide calibrated evidence of biomass productivity, oxygen generation, CO_2 fixation, or system-level energy performance [62], [63]. These limitations define the principal validation tasks required before the proposed concept can be considered for façade-scale implementation.

Accordingly, future development should prioritize standardized building-envelope testing and long-term operational validation rather than simply increasing geometric or control complexity. Structural performance, watertightness, durability, optical behaviour, hydraulic operation, biological stability, energy demand, maintenance, and safety should be evaluated together to determine whether the proposed module can progress from a functional prototype toward a viable building-integrated bio-reactive façade component.

8. Conclusions

This study demonstrates the prototype-level building-engineering feasibility of additively manufactured PETG microalgal curtain-wall modules. Nine parametrically differentiated geometries were fabricated using a common continuous single-wall strategy. Despite morphological variation, predicted filament demand remained highly consistent, with a coefficient of variation of 0.87%, while recorded printing times ranged from 100 to 125 min under a common accelerated operating mode. These results demonstrate that controlled geometric differentiation can be achieved while maintaining relatively stable fabrication demand within the investigated design space.

Transparent PETG prototypes further demonstrated basic liquid containment, pump-driven circulation with *Spirulina* (*Arthrospira*)-containing culture medium, and preliminary multi-module assembly. The embedded monitoring-and-control subsystem provided sensing, state processing, local visualization, and rule-based circulation-pump actuation, supporting the transition from an additively manufactured reactor vessel toward an operational and modular bio-reactive façade prototype.

The current system remains a proof-of-concept rather than a validated building-scale curtain-wall solution. Standardized watertightness, structural performance, durability, weathering, fire safety, optical behaviour, hydraulic performance, biological productivity, energy demand, and long-term operation remain to be quantitatively assessed. Future work should therefore focus on integrated façade-scale performance validation to determine the viability of the proposed modules as building-integrated bio-reactive envelope components.

Funding

This research received no external funding.

Authors' contributions

Sheng Bi conceived the study, developed the research methodology, conducted the parametric design and additive-manufacturing experiments, performed the formal analysis, integrated the prototype system, curated the data, prepared the figures, and drafted the manuscript. Yucheng Guo contributed to methodology development, validation, data interpretation, and manuscript revision. Mingyang Feng contributed to fabrication support, experimental implementation, and data collection. Yulong Chen contributed to computational design, visualization, and manuscript revision. Xinyi Zheng contributed to data analysis, visualization, and manuscript revision. Lingxiao Chen contributed to methodology, validation, and manuscript revision. Cossima Cornadó Bardón contributed to supervision, conceptual development, and critical revision of the manuscript. Zeyu Chao supervised the overall research, coordinated the study, contributed to methodology development, validation, and interpretation of the results,

and critically reviewed and revised the manuscript. Dingwen Bao contributed to conceptualization, methodological guidance, academic supervision, project administration, and critical revision of the manuscript. Oriol Pons Valladares provided academic supervision, research guidance, and critical revision of the manuscript. All authors reviewed and approved the final manuscript.

Data availability

The geometric data, slicer-derived fabrication estimates, and recorded printing times supporting the findings of this study are reported in the manuscript. Additional underlying experimental records and prototype documentation are available from the corresponding author upon reasonable request.

Code availability

The firmware code supporting the STM32-based sensing, signal processing, and circulation-pump control described in this study is available from the corresponding author upon reasonable request.

Competing interests

The authors declare no competing interests.

References

[1] S. LIU, G. Chen, J. Li, and S. Cao, “Smart Skin for Zero Energy Buildings: A Review of Thermoresponsive Spectral-Adaptive Envelopes,” *Advanced Materials*, vol. 38, no. 3, Jan. 2026, doi: 10.1002/adma.202511392.

[2] G. Jamilu, A. Abdou, and M. Asif, “Dynamic facades for sustainable buildings: A review of classification, applications, prospects and challenges,” *Energy Reports*, vol. 11, pp. 5999–6014, Jun. 2024, doi: 10.1016/j.egyr.2024.05.047.

[3] R. C. G. M. Loonen, F. Favoino, J. L. M. Hensen, and M. Overend, “Review of current status, requirements and opportunities for building performance simulation of adaptive facades,” *J. Build. Perform. Simul.*, vol. 10, no. 2, pp. 205–223, Mar. 2017, doi: 10.1080/19401493.2016.1152303.

[4] M. Talaei and A. Prieto, “A review on performance of sustainable microalgae photobioreactor façades technology: exploring challenges and advantages,” *Archit. Sci. Rev.*, vol. 67, no. 5, pp. 387–414, Sep. 2024, doi: 10.1080/00038628.2024.2305889.

[5] M. Talaei, M. Mahdavinejad, R. Azari, H. M. Haghighi, and A. Atashdast, “Thermal and energy performance of a user-responsive microalgae bioreactive façade for climate

826 adaptability," *Sustainable Energy Technologies and Assessments*, vol. 52, p. 101894,
827 Aug. 2022, doi: 10.1016/j.seta.2021.101894.

828 [6] V. Pozzobon, "Microalgae bio-reactive façade: A model coupling weather, illumination,
829 temperature, and cell growth over the year," *Renew. Energy*, vol. 237, p. 121545, Dec.
830 2024, doi: 10.1016/j.renene.2024.121545.

831 [7] K. H. Kim, M. W. Parrow, and P. Kheirkhah Sangdeh, "Microalgae-integrated building
832 enclosures: a nature-based solution for carbon sequestration," *Front. Built Environ.*,
833 vol. 11, May 2025, doi: 10.3389/fbuil.2025.1574582.

834 [8] M. R. Villalba Yépez, R. Cervera Sardá, and F. J. Sánchez Alejo, "Innovative urban
835 sustainability: Low-maintenance photobioreactor façades in architectural design," in
836 *Advances in Bio-Based Materials for Construction and Energy Efficiency*, Elsevier,
837 2025, pp. 565–587. doi: 10.1016/B978-0-443-32800-8.00020-2.

838 [9] H. Shahamat, "Advancing bio-integrated building systems: a systematic review of
839 architectural, structural and mechanical–electrical challenges in photobioreactor
840 façades," *Smart and Sustainable Built Environment*, pp. 1–32, Aug. 2025, doi:
841 10.1108/SASBE-03-2025-0156.

842 [10] E. S. Umdu, İ. Kahraman, N. Yildirim, and L. Bilir, "Optimization of microalgae panel
843 bioreactor thermal transmission property for building façade applications," *Energy*
844 *Build.*, vol. 175, pp. 113–120, Sep. 2018, doi: 10.1016/j.enbuild.2018.07.027.

845 [11] M. T. Araji and I. Shahid, "Symbiosis optimization of building envelopes and micro-
846 algae photobioreactors," *Journal of Building Engineering*, vol. 18, pp. 58–65, Jul. 2018,
847 doi: 10.1016/j.jobe.2018.02.008.

848 [12] S. Vajdi and A. Aslani, "Design and techno-economic analysis of direct CO2 capturing
849 with integrated photobioreactors as a building façade," *Sustainable Energy*
850 *Technologies and Assessments*, vol. 56, p. 103068, Mar. 2023, doi:
851 10.1016/j.seta.2023.103068.

852 [13] S. Nazari, I. Sheikhansari, P. Keshavarz Mirzamohammadi, F. Mirnataj, and B. Sajadi,
853 "Impact of microalgae-integrated windows on building performance: Energy, daylight,
854 and carbon analysis using an innovative simulation method," *Energy Reports*, vol. 15,
855 p. 108905, Jun. 2026, doi: 10.1016/j.egyr.2025.12.042.

856 [14] V. Piccioni *et al.*, "Tuning the Solar Performance of Building Facades through Polymer
857 3D Printing: Toward Bespoke Thermo-Optical Properties," *Adv. Mater. Technol.*, vol. 8,
858 no. 6, Mar. 2023, doi: 10.1002/admt.202201200.

859 [15] S. Na, S. Kim, and S. Moon, "Additive manufacturing (3D Printing)-applied

construction: Smart node system for an irregular building façade," *Journal of Building Engineering*, vol. 56, p. 104743, Sep. 2022, doi: 10.1016/j.jobe.2022.104743.

[16] S. Lim, R. A. Buswell, T. T. Le, S. A. Austin, A. G. F. Gibb, and T. Thorpe, "Developments in construction-scale additive manufacturing processes," *Autom. Constr.*, vol. 21, pp. 262–268, Jan. 2012, doi: 10.1016/j.autcon.2011.06.010.

[17] D.-R. Baraboi *et al.*, "Smart 3D-printed facades: a review of innovations, materials, and sustainable performance," *Frontiers in Sustainable Cities*, vol. 7, Jul. 2025, doi: 10.3389/frsc.2025.1610729.

[18] G. Gaal *et al.*, "Simplified fabrication of integrated microfluidic devices using fused deposition modeling 3D printing," *Sens. Actuators B Chem.*, vol. 242, pp. 35–40, Apr. 2017, doi: 10.1016/j.snb.2016.10.110.

[19] M. Kazemi, M. Shahsavari, and B. Houshmand, "A Parametric Study on the Hydrothermal Stability of Fused Deposition Modeled Polylactic Acid: The Interactive Effects of Nozzle Temperature, Layer Thickness, and Wall Count," *J. Mater. Eng. Perform.*, vol. 35, no. 26, pp. 26263–26274, Jul. 2026, doi: 10.1007/s11665-026-13544-4.

[20] E. G. Nwoba, D. Chuka-Ogwude, A. Vadiveloo, and J. C. Ogbonna, "Process control strategies applied to microalgae-based biofuel production," in *3rd Generation Biofuels*, Elsevier, 2022, pp. 105–134. doi: 10.1016/B978-0-323-90971-6.00031-0.

[21] P. Erbland, S. Caron, M. Peterson, and A. Alyokhin, "Design and performance of a low-cost, automated, large-scale photobioreactor for microalgae production," *Aquac. Eng.*, vol. 90, p. 102103, Aug. 2020, doi: 10.1016/j.aquaeng.2020.102103.

[22] B. Dokhaei, A. Alipour, K. Abdelaziz, B. Shafei, P. Sarkar, and J. Hobeck, "Cyber-physical smart morphing facades driven by reinforcement learning for wind-induced vibration control in tall buildings," *Journal of Wind Engineering and Industrial Aerodynamics*, vol. 273, p. 106394, Jun. 2026, doi: 10.1016/j.jweia.2026.106394.

[23] J. Böke, U. Knaack, and M. Hemmerling, "Automated adaptive façade functions in practice - Case studies on office buildings," *Autom. Constr.*, vol. 113, p. 103113, May 2020, doi: 10.1016/j.autcon.2020.103113.

[24] Z. Zuo *et al.*, "Systematic workflow for digital design and on-site 3D printing of large concrete structures: A case study of a full-size two-story building," *Journal of Building Engineering*, vol. 104, p. 112370, Jun. 2025, doi: 10.1016/j.jobe.2025.112370.

[25] A. Gamal, B. Nashaat, M. M. Shahda, and S. R. Nosier, "Ten questions concerning the integration of digital fabrication techniques into the architectural design process,"

Architectural Engineering and Design Management, vol. 20, no. 1, pp. 120–149, Jan. 2024, doi: 10.1080/17452007.2023.2269559.

[26] E. S. Barjuei, A. Capitanelli, R. Bertolucci, E. Courteille, F. Mastrogiovanni, and M. Maratea, "Digital workflow for printability checking and prefabrication in robotic construction 3D printing based on Artificial Intelligence planning," *Eng. Appl. Artif. Intell.*, vol. 133, p. 108254, Jul. 2024, doi: 10.1016/j.engappai.2024.108254.

[27] G. M. Elrayies, "Microalgae: Prospects for greener future buildings," *Renewable and Sustainable Energy Reviews*, vol. 81, pp. 1175–1191, Jan. 2018, doi: 10.1016/j.rser.2017.08.032.

[28] J. Pruvost, B. Le Gouic, O. Lepine, J. Legrand, and F. Le Borgne, "Microalgae culture in building-integrated photobioreactors: Biomass production modelling and energetic analysis," *Chemical Engineering Journal*, vol. 284, pp. 850–861, Jan. 2016, doi: 10.1016/j.cej.2015.08.118.

[29] R. Elsayed, M. I. Ismail, A. F. Ashour, H. A. Sakr, M. I. Ibrahem, and M. M. Fouda, "A Review of Smart Building Management Systems: CPS Applications for Energy-Efficient Monitoring and Control," in *2025 3rd International Conference on Artificial Intelligence, Blockchain, and Internet of Things (AIBThings)*, IEEE, Sep. 2025, pp. 1–6. doi: 10.1109/AIBThings66987.2025.11296174.

[30] A. Bonci, A. Carbonari, A. Cucchiarelli, L. Messi, M. Pirani, and M. Vaccarini, "A cyber-physical system approach for building efficiency monitoring," *Autom. Constr.*, vol. 102, pp. 68–85, Jun. 2019, doi: 10.1016/j.autcon.2019.02.010.

[31] D. Briels *et al.*, "Monolithic AM façade: multi-objective parametric design optimization of additively manufactured insulating wall elements," *Front. Built Environ.*, vol. 9, Oct. 2023, doi: 10.3389/fbuil.2023.1286933.

[32] G. Yan, Y. Jia, M. Zhen, and Q. Dong, "Integrated design and fabrication of additive manufacturing-based shading components with daylight performance optimization," *Journal of Building Engineering*, vol. 114, p. 114416, Nov. 2025, doi: 10.1016/j.jobe.2025.114416.

[33] J. Liu *et al.*, "Current and future trends in topology optimization for additive manufacturing," *Structural and Multidisciplinary Optimization*, vol. 57, no. 6, pp. 2457–2483, Jun. 2018, doi: 10.1007/s00158-018-1994-3.

[34] A. T. Gaynor and J. K. Guest, "Topology optimization considering overhang constraints: Eliminating sacrificial support material in additive manufacturing through design," *Structural and Multidisciplinary Optimization*, vol. 54, no. 5, pp. 1157–1172, Nov.

2016, doi: 10.1007/s00158-016-1551-x.

[35] X. Chen, G. Fang, W.-H. Liao, and C. C. L. Wang, “Field-Based Toolpath Generation for 3D Printing Continuous Fibre Reinforced Thermoplastic Composites,” *Addit. Manuf.*, vol. 49, p. 102470, Jan. 2022, doi: 10.1016/j.addma.2021.102470.

[36] F. Xie *et al.*, “Printing path optimization of continuous fiber additive manufacturing based on manufacturing-constrained stress alignment field,” *Compos. Struct.*, vol. 385, p. 120208, Jun. 2026, doi: 10.1016/j.compstruct.2026.120208.

[37] J. R. Kubalak, A. L. Wicks, and C. B. Williams, “Simultaneous topology and toolpath optimization for layer-free multi-axis additive manufacturing of 3D composite structures,” *Addit. Manuf.*, vol. 104, p. 104774, Apr. 2025, doi: 10.1016/j.addma.2025.104774.

[38] G. M. Fortunato, M. Nicoletta, E. Batoni, G. Vozzi, and C. De Maria, “A fully automatic non-planar slicing algorithm for the additive manufacturing of complex geometries,” *Addit. Manuf.*, vol. 69, p. 103541, May 2023, doi: 10.1016/j.addma.2023.103541.

[39] A. Gleadall, “FullControl GCode Designer: Open-source software for unconstrained design in additive manufacturing,” *Addit. Manuf.*, vol. 46, p. 102109, Oct. 2021, doi: 10.1016/j.addma.2021.102109.

[40] L. Breseghello and R. Naboni, “Toolpath-based design for 3D concrete printing of carbon-efficient architectural structures,” *Addit. Manuf.*, vol. 56, p. 102872, Aug. 2022, doi: 10.1016/j.addma.2022.102872.

[41] M. Takhmasib, H. J. Lee, and H. Yi, “Machine-learned kinetic Façade: Construction and artificial intelligence enabled predictive control for visual comfort,” *Autom. Constr.*, vol. 156, p. 105093, Dec. 2023, doi: 10.1016/j.autcon.2023.105093.

[42] G. Chiesa, D. Di Vita, A. Ghadirzadeh, A. H. Muñoz Herrera, and J. C. Leon Rodriguez, “A fuzzy-logic IoT lighting and shading control system for smart buildings,” *Autom. Constr.*, vol. 120, p. 103397, Dec. 2020, doi: 10.1016/j.autcon.2020.103397.

[43] L. Morales Escobar, J. Aguilar, A. Garces-Jimenez, J. A. Gutierrez De Mesa, and J. M. Gomez-Pulido, “Advanced Fuzzy-Logic-Based Context-Driven Control for HVAC Management Systems in Buildings,” *IEEE Access*, vol. 8, pp. 16111–16126, 2020, doi: 10.1109/ACCESS.2020.2966545.

[44] S. Goyal, H. A. Ingley, and P. Barooah, “Occupancy-based zone-climate control for energy-efficient buildings: Complexity vs. performance,” *Appl. Energy*, vol. 106, pp. 209–221, Jun. 2013, doi: 10.1016/j.apenergy.2013.01.039.

[45] "Test Method for Field Determination of Water Penetration of Installed Exterior Windows, Skylights, Doors, and Curtain Walls, by Uniform or Cyclic Static Air Pressure Difference," Feb. 01, 2023, *ASTM International, West Conshohocken, PA*. doi: 10.1520/E1105-15R23.

[46] S. Ma, Y. Huang, X. Zhu, A. Xia, X. Zhu, and Q. Liao, "Growth-based dynamic light transmission modeling and optimization in microalgal photobioreactors for high efficiency CO2 fixation," *Renewable and Sustainable Energy Reviews*, vol. 197, p. 114414, Jun. 2024, doi: 10.1016/j.rser.2024.114414.

[47] E. Yahaya, W. S. Yeo, and J. Nandong, "Optimization of microalgae cultivation and CO2 capture in a three-stage bubble column photobioreactor: Evaluation of control strategies," *Process Safety and Environmental Protection*, vol. 196, p. 106906, Apr. 2025, doi: 10.1016/j.psep.2025.106906.

[48] H. H. Ngo *et al.*, "Advances of Photobioreactors in Wastewater Treatment: Engineering Aspects, Applications and Future Perspectives," 2019, pp. 297–329. doi: 10.1007/978-981-13-3259-3_14.

[49] A. F. M. de Mello *et al.*, "Strategies and engineering aspects on the scale-up of bioreactors for different bioprocesses," *Systems Microbiology and Biomanufacturing*, vol. 4, no. 2, pp. 365–385, Apr. 2024, doi: 10.1007/s43393-023-00205-z.

[50] S. Salta, N. Papavasileiou, K. Pyliotis, and M. Katsaros, "Adaptable emergency shelter: A case study in generative design and additive manufacturing in mass customization era," *Procedia Manuf.*, vol. 44, pp. 124–131, 2020, doi: 10.1016/j.promfg.2020.02.213.

[51] P. Wu, J. Wang, and X. Wang, "A critical review of the use of 3-D printing in the construction industry," *Autom. Constr.*, vol. 68, pp. 21–31, Aug. 2016, doi: 10.1016/j.autcon.2016.04.005.

[52] S. Berretta, R. Davies, Y. T. Shyng, Y. Wang, and O. Ghita, "Fused Deposition Modelling of high temperature polymers: Exploring CNT PEEK composites," *Polym. Test.*, vol. 63, pp. 251–262, Oct. 2017, doi: 10.1016/j.polymertesting.2017.08.024.

[53] J. Allum, A. Moetazedian, A. Gleadall, and V. V. Silberschmidt, "Interlayer bonding has bulk-material strength in extrusion additive manufacturing: New understanding of anisotropy," *Addit. Manuf.*, vol. 34, p. 101297, Aug. 2020, doi: 10.1016/j.addma.2020.101297.

[54] J. Böke, U. Knaack, and M. Hemmerling, "Prototype of a cyber-physical façade system," *Journal of Building Engineering*, vol. 31, p. 101397, Sep. 2020, doi:

10.1016/j.jobe.2020.101397.

[55] A. L. Cheng, G. Latorre, L. F. Amores, M. T. Paucar, and A. Mena, “Enhancement of an Adaptive Building-Skin System for Local and Remote Multi-Modal Operation,” in *2024 IEEE Eighth Ecuador Technical Chapters Meeting (ETCM)*, IEEE, Oct. 2024, pp. 1–6. doi: 10.1109/ETCM63562.2024.10746014.

[56] I. M. L. Pataro, J. D. Gil, J. L. Guzmán, M. Berenguel, and J. M. Lemos, “A learning-based model predictive strategy for pH control in raceway photobioreactors with freshwater and wastewater cultivation media,” *Control Eng. Pract.*, vol. 138, p. 105619, Sep. 2023, doi: 10.1016/j.conengprac.2023.105619.

[57] P. Otálora, S. Banerjee, M. El Mistiri, O. Khan, D. E. Rivera, and J. L. Guzmán, “Enhancing pH control in microalgae raceway photobioreactors using 3DoF-KF model-on-demand model predictive control,” *Control Eng. Pract.*, vol. 168, p. 106742, Mar. 2026, doi: 10.1016/j.conengprac.2025.106742.

[58] I. Cheibas *et al.*, “3D printing of a multi-performative building envelope: Assessment of air permeability, water tightness, wind loads, and impact resistance,” *Journal of Building Engineering*, vol. 98, p. 111251, Dec. 2024, doi: 10.1016/j.jobe.2024.111251.

[59] G. Grassi, S. Lupica Spagnolo, and I. Paoletti, “Fabrication and durability testing of a 3D printed façade for desert climates,” *Addit. Manuf.*, vol. 28, pp. 439–444, Aug. 2019, doi: 10.1016/j.addma.2019.05.023.

[60] A. Afshar and D. Mihut, “Enhancing durability of 3D printed polymer structures by metallization,” *J. Mater. Sci. Technol.*, vol. 53, pp. 185–191, Sep. 2020, doi: 10.1016/j.jmst.2020.01.072.

[61] R. Naboni and N. Jakica, “Additive manufacturing in skin systems: trends and future perspectives,” in *Rethinking Building Skins*, Elsevier, 2022, pp. 425–451. doi: 10.1016/B978-0-12-822477-9.00004-8.

[62] N. Biloria and Y. Thakkar, “Integrating algae building technology in the built environment: A cost and benefit perspective,” *Frontiers of Architectural Research*, vol. 9, no. 2, pp. 370–384, Jun. 2020, doi: 10.1016/j.foar.2019.12.004.

[63] X. Lu, S. Guo, Z. Mao, Y. Li, H. Liu, and X. Zhao, “Carbon-Swallow Photovoltaic Modules—Perspective overview and preliminary study,” *Sci. China Technol. Sci.*, vol. 69, no. 9, p. 1920102, Sep. 2026, doi: 10.1007/s11431-026-3445-3.